

www.acsami.org Research Article

Low-Frequency Raman Study of Large-Area Twisted Bilayers of WS₂ Stacked by an Etchant-Free Transfer Method

Manpreet Boora, Yu-Chuan Lin, Chen Chen, Nicholas Trainor, Joshua A. Robinson, Joan M. Redwing, and Jae Yong Suh*



Cite This: ACS Appl. Mater. Interfaces 2024, 16, 2902-2911



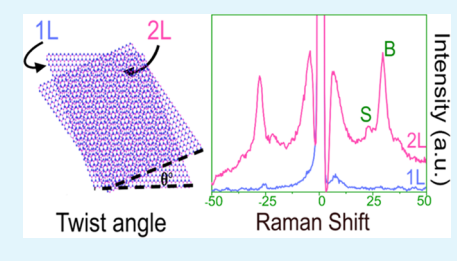
ACCESS I

Metrics & More

Article Recommendations

s Supporting Information

ABSTRACT: Monolayer transition metal dichalcogenides have strong intracovalent bonding. When stacked in multilayers, however, weak van der Waals interactions dominate interlayer mechanical coupling and, thus, influence their lattice vibrations. This study presents the frequency evolution of interlayer phonons in twisted WS₂ bilayers, highly subject to the twist angle. The twist angle between the layers is controlled to modulate the spacing between the layers, which, in turn, affects the interlayer coupling that is probed by Raman spectroscopy. The shifts of high-frequency E_{2g}^1 (Γ) and A_{1g} (Γ) phonon modes and their frequency separations are dependent on the twist angle, reflecting the correlation between the interlayer mechanical coupling



and twist angle. In this work, we fabricated large-area, twisted bilayer WS_2 with a clean interface with controlled twist angles. Polarized Raman spectroscopy identified new interlayer modes, which were not previously reported, depending on the twist angle. The appearance of breathing modes in Raman phonon spectra provides evidence of strong interlayer coupling in bilayer structures. We confirm that the twist angle can alter the exciton and trion dynamics of bilayers as indicated by the photoluminescence peak shift. These large-area controlled twist angle samples have practical applications in optoelectronic device fabrication and twistronics.

KEYWORDS: two-dimensional materials, moiré phonons, low-frequency phonons, interlayer coupling, Raman spectra, exciton dynamics, bilayer WS_2

1. INTRODUCTION

The discovery of flat bands at the magic angle of 1.1° in twisted graphene systems brought about rich studies of correlated insulating states and unconventional superconductivity and also inspired the search for similar properties in other stacked two-dimensional (2D) materials. 2D transition metal dichalcogenides (TMDs) remain one of the prominent candidates for this search. TMDs are a class of semiconductor compounds denoted by MX₂, where M is a transition metal atom sandwiched by two chalcogen (X) atoms in a hexagonal crystalline structure. They have an intriguing set of properties including but not limited to atomic-scale thickness, a direct band gap for the monolayer in the visible region, strong spinorbit coupling, and a strong nonlinear response such as secondharmonic generation (SHG).²⁻⁴ These characteristics make the study of TMDs very interesting and invaluable to the fields of optoelectronics, spintronics, energy harvesting, and nanoelectronics. 5,6 Monolayers of the same or different constituent materials can be stacked together to form bilayers of TMDs. The stacking can be performed at various angles between the crystal axes of two monolayers, called the twist angle. The additional degrees of freedom created by this bilayer stacking opened various possibilities to control the optical and electronic properties of TMDs.

The tungsten disulfide (WS₂) monolayer (ML) is an interesting 2D TMD that exhibits some unique properties

such as strong Coulomb binding effects, tunability of the band gap in the visible region, quantum confinement, and the largest spin—orbit coupling of about 0.4 eV. Furthermore, due to the reduced effective carrier mass, the WS $_2$ ML has a high electron mobility of 100 cm $^2/({\rm V~s})$ among other semiconducting 2D TMDs. These properties make the WS $_2$ ML an ideal candidate for studying the interplay of spin—orbit coupling, interlayer coupling, and phonons with the degree of freedom of the twist angle in the bilayers of TMDs. 10,11

The stacking of two or more individual MLs leads to the emergence of the interlayer exciton, where the electron and hole are spatially located in different monolayers. The twist angle between the individual MLs of TMDs while stacking can greatly influence the strength of interlayer excitons. In twisted bilayer TMDs, where the electronic bands of the constituent monolayers are energetically degenerate, the interlayer hybridization becomes dominant and significantly modifies the bilayer eigenstates depending on the twist angle. Understanding the interlayer interactions of such artificially

Received: October 2, 2023
Revised: December 8, 2023
Accepted: December 21, 2023
Published: January 3, 2024





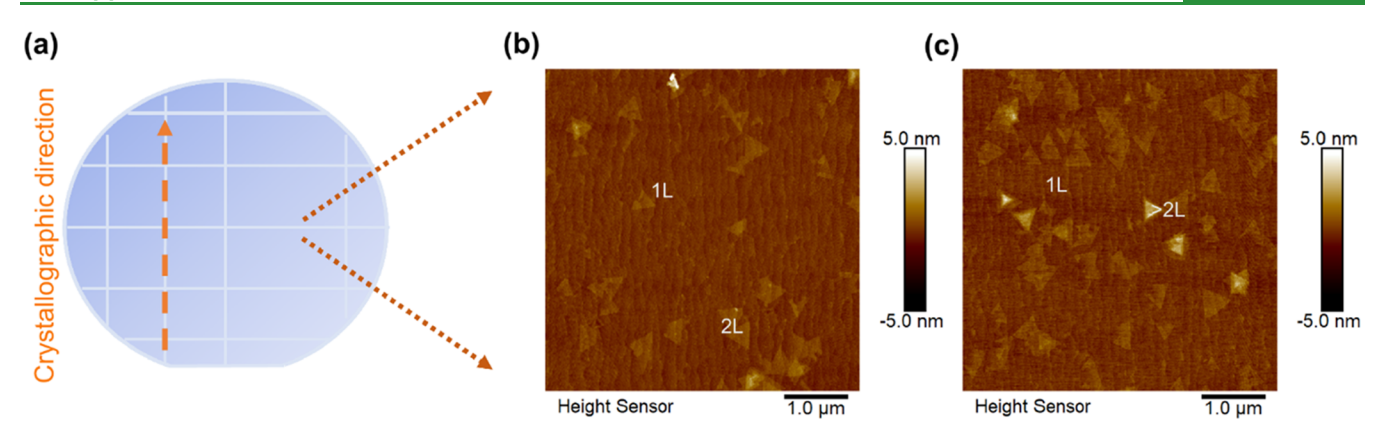


Figure 1. (a) As-grown WS₂ monolayer (marked as 1L) deposited on the 2 in. scribed c-plane sapphire wafer. AFM images of the as-grown WS₂ at (b) center and (c) edge regions confirm the high-quality coalesced monolayer with few bilayer (2L) islands.

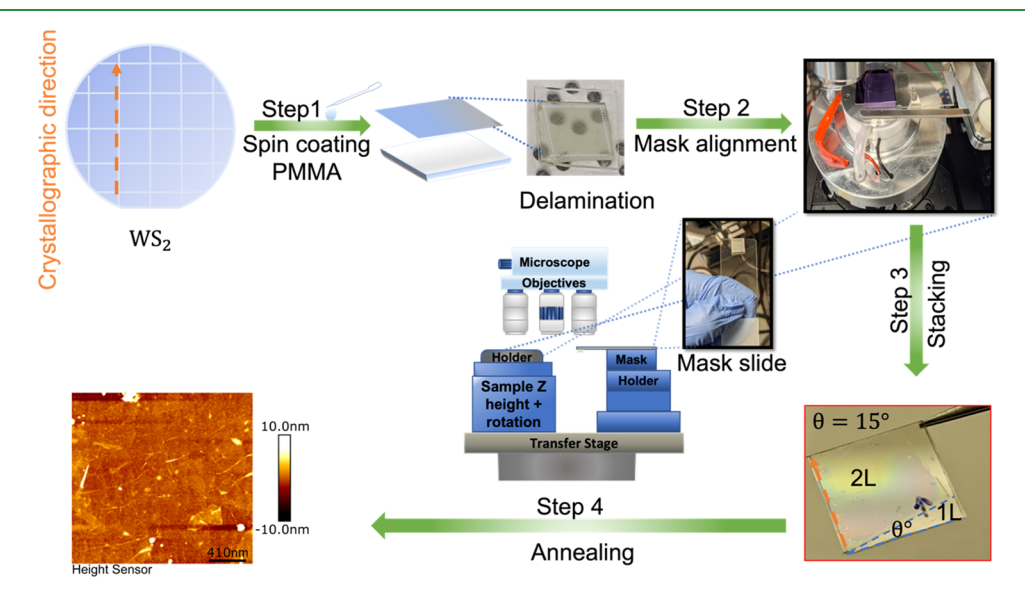


Figure 2. Schematic of the transfer process for fabricating large-area stacked twisted bilayers of WS₂ with precise control of the twist angle. The multiple steps involved coating with PMMA, delamination, mask alignment, stacking, and annealing.

formed van der Waals (vdWs) structures is fundamentally important, as it provides new insights into enhancing the performances of potential optoelectronic devices.

When there is either a relative twist angle or a difference in the lattice constant for the two periodic patterns, long moiré period superlattices emerge. Recently, moiré superlattices of semiconducting property have attracted interest as a potentially simpler and more robust platform for simulating the Hubbard model on an emergent lattice. Vibrational properties and the band structures depend on the twist angle because of the strain or buckling of chalcogen atoms changing. 14,15 For twisted TMDs, the phonon vibrational properties and the band structures depend on the twist angle because the strain or buckling of chalcogen atoms changes the interlayer distances. The moiré patterns in vdWs structures create a periodic potential based on the interlayer interactions, which can impose modulation on the electronic structures of the constituents. For example, interlayer coupling strength and the number of flat moiré bands increase at small twist angles, and the Dirac velocity of quasi-particles becomes zero. 13,1

In this work, we present an experimental study of low-frequency Raman modes and moiré phonons, which can be used to probe the strength and dependence of interlayer coupling on the twist angle in homobilayer WS₂. We fabricated

large-area WS_2 bilayers by applying an etchant and solution-free transfer of as-grown WS_2 MLs. Then, we conducted a detailed study of optical, polarized Raman scattering, and photoluminescence (PL) spectroscopic measurements to uncover the relationship between the stacking angle and interface coupling of twisted bilayers. Our work may provide insights into moiré physics, as moiré phonons are extremely sensitive to layer twisting. The twist angle can change the interlayer separation between the monolayers of a stacked WS_2 bilayer and can be used to infer the interfacial coupling, which is associated with a change in PL and shifts in the band gap and Raman modes.

2. RESULTS AND DISCUSSION

2.1. Synthesis and Fabrication. This section describes the experimental methods used to fabricate and characterize single-crystal, large-area, high-quality samples of bilayer WS₂. Only a few studies have considered the stacking of epitaxial films of TMDs transferred from large-area films of epitaxial-grown MoS_2 with controlled twist angles¹⁷ and demonstrated the dependence of their electrical properties on the twist angle. The reason for such few studies might be attributed to the numerous challenges, such as precise control of the twist angle,

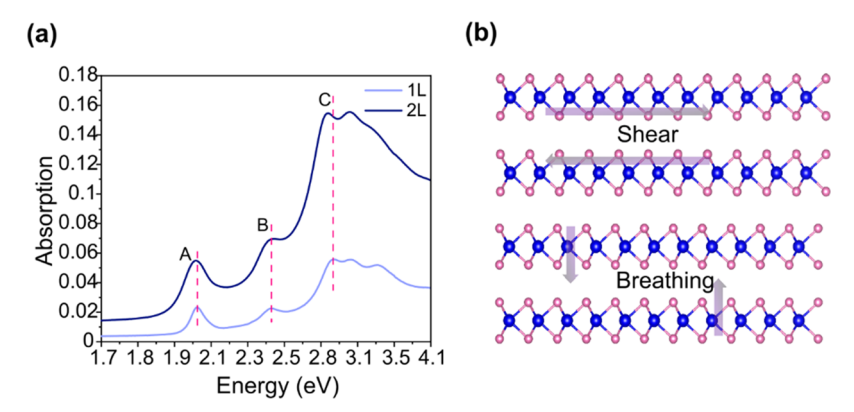


Figure 3. (a) Optical absorption spectra show dominant excitons present in the spectra of ML and BL WS₂. (b) Intralayer lattice vibration modes are present in BLs.

the size of the transferred film, and different surface energies of TMDs, resulting in weak adhesion between constituent layers and substrates. 18

Figure 1 shows epitaxially grown films of WS₂ using the procedure described in Section 4. The wafer-scale WS2 films require epitaxial growth and coalescence of oriented domains to form a continuous monolayer. The monolayer WS2 used in preparing vdWs structures was grown by the MOCVD method on 2 in.-diameter *c*-plane sapphire substrates. Chubarov et al. report that well-defined parallel steps on sapphire substrate guide TMD domains to align in one direction during the nucleation stage of growth, and later, these domains coalesce into a single film during the ripening stage. 19 Transmission electron microscopy analysis confirmed coalesced single-crystal regions with the same crystallographic direction and largely free of inverse domain boundaries. Furthermore, electron diffraction also confirmed that WS2 monolayers were singlecrystalline. 19 The crystallographic direction (c-plane) of the sapphire substrate leads to the epitaxial alignment of WS2 domains that coalesce into a continuous film. Figure 1a shows the predetermined crystallographic direction of the coalesced regions. Figure 1b,c shows the atomic force microscopy (AFM) images of the complete coverage of the WS₂ ML and a few small bilayer (BL) islands. The AFM confirmed the high quality of monolayer WS₂ as indicated by a complete absence of pinholes, bubbles, or cracks in the film.

Figure 2 shows the etchant-free transfer of the film, which is a crucial process for obtaining clean bilayer interfaces. In the first step, a layer of PMMA was coated on the WS2 film, followed by thermal treatment at 130 °C for cross-linking of PMMA with the film. Next, poly(dimethylsiloxane) (PDMS) and deionized water were used as transferring medium and full delamination (peeling off) of WS₂ films from the sapphire substrates. Since the sapphire substrate is hydrophilic and the TMD films are hydrophobic, these contact forces of action can separate the film from the substrate, and the film floats on water. In the second step, a mask slide was prepared with the delaminated film, and a target substrate was placed on the transfer stage along the known crystallographic direction. In the third step, by the controlled movement of the stage in the z-direction, the substrate was brought close to the mask slide while keeping the x and y directions fixed. The bottom substrate is kept fixed, and then, the second layer is aligned and oriented along the sharp edge to achieve a precise twist angle. After the interfacial contact between the two layers was achieved, the stage was heated to soften the PDMS and thus

release the film, followed by annealing in an argon flow at 400 °C for 4 h. Other studies used acetone to remove PMMA, which left a visible amount of residue on the transferred films, causing the creation of undesirable pores in the films. 20,21 To avoid unnecessary pores or cracks in step four, we make use of annealing in a controlled environment to improve the interactions between the two stacked layers. WS2 was grown on a scored sapphire wafer using a high-precision dicing saw to make sure that the cut sapphire had maximum parallel alignment. The crystal axis of the transferred WS₂ layer was with the sharp edge of the monolayer sitting on a sapphire substrate. The top layer is oriented relative to the bottom layer using a motorized transfer system (HQ Graphene, HQ2D MOT) whose built-in software optically determines the best alignment and final twist angle of the two edges during realtime stacking. The edges of each layer are very straight and sharp, ensuring high accuracy of the twist angle, as seen in the optical image of bilayer WS₂ (see Figure S1). The AFM image demonstrates that the surfaces of all of the transferred films are clean and uniform. This transfer method provides a clean interface between the two TMD layers that are never exposed to any chemical and thus show much less PMMA residue on the transferred layer.

2.2. Absorption Measurements. The optical properties of TMDs are dominated by tightly bound electron-hole pairs (excitons) and lattice vibration modes (phonons). Strong exciton-phonon interactions can result in the enhanced intensity of phonon modes close to the Rayleigh background. Figure 3a shows the optical absorption spectra of monolayers and stacked bilayers of WS₂. In the absorption spectrum of the WS₂ ML, two peaks corresponding to the A exciton at 2 eV and the B exciton at 2.39 eV are present due to the interband dipole-allowed exciton transitions. In contrast, a broad peak around 2.86 eV for the C exciton is observed due to the transitions between the highest valence band and the first three lowest conduction bands around the Γ -point of the Brillouin zone.²² Figure S3 in the Supporting Information shows the optical absorption spectra, including different cases of the twist angle in the bilayer. On transitioning from the ML to the BL, the absorption intensity of bilayer WS₂ increases by 8% because of the band nesting (conduction and valence bands are parallel to each other) near C excitons. The band nesting results in a strong light-matter interaction²³ and causes the van Hove singularity feature, which are saddle points of energy dispersion in the k-space in the joint density of states.²⁴

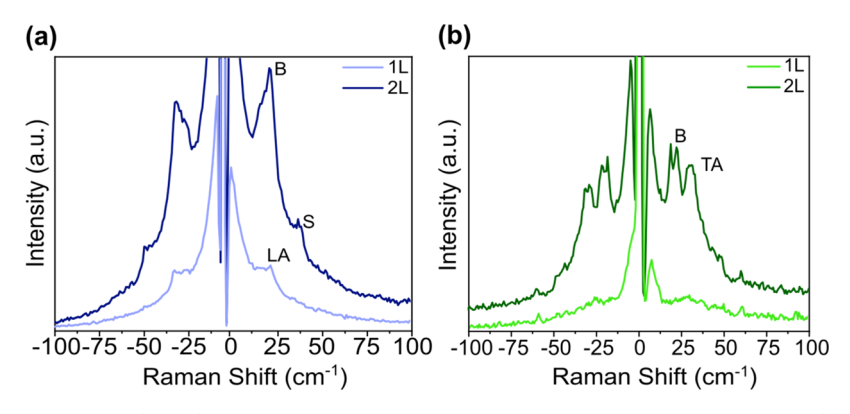


Figure 4. Low-frequency Raman spectra (LFRS) of ML and BL WS₂ without a twist angle with laser excitation at (a) 532 nm (2.34 eV) and (b) 488 nm (2.54 eV). Each spectrum is an average of at least two locations on the sample.

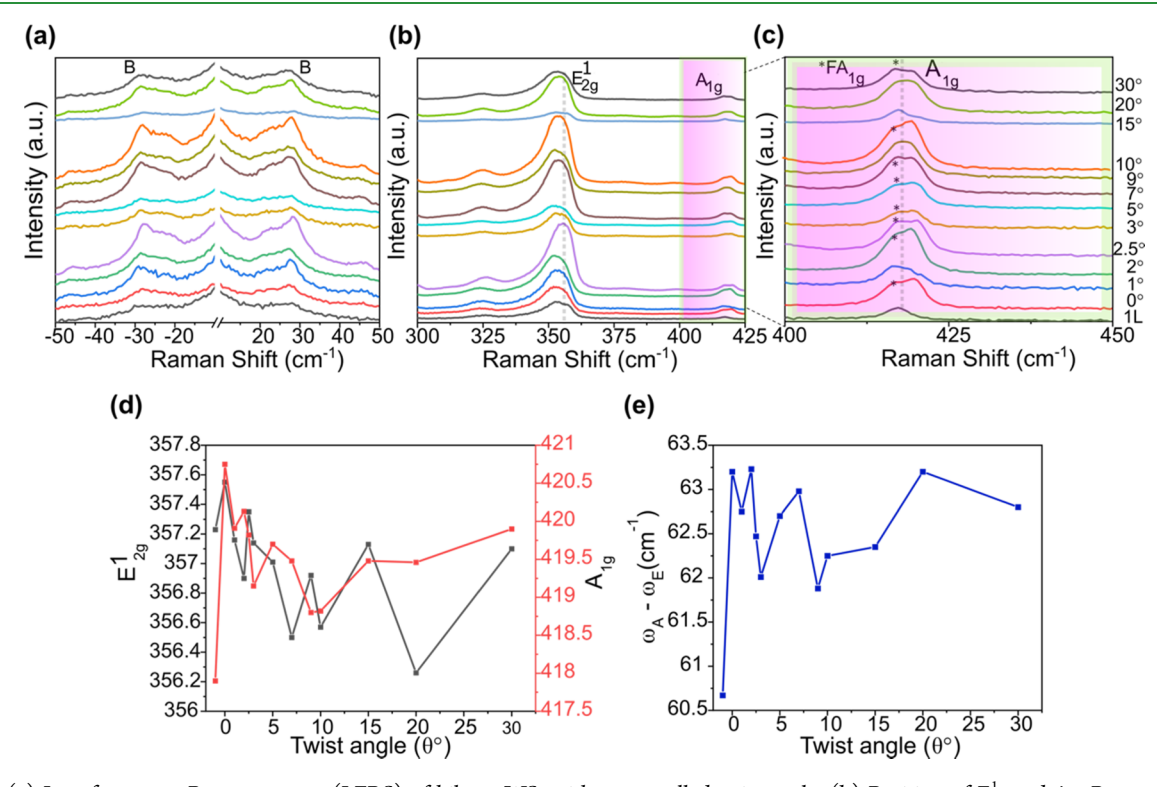


Figure 5. (a) Low-frequency Raman spectra (LFRS) of bilayer WS_2 with a controlled twist angle. (b) Position of E^1_{2g} and A_{1g} Raman peaks as a function of the twist angle. (c) Spectra are normalized to the Si peak and vertically offset for clarity. Part of the spectra indicated by a pink area rectangle in (b) is zoomed, and FA_{1g} peaks marked by asterisks indicate the moiré phonons (d) Position of the E^1_{2g} and A_{1g} Raman peaks as a function of the twist angle. (e) Frequency separation between E^1_{2g} and A_{1g} at various twist angles with laser excitation at 532 nm (2.54 eV).

With the change in the band gap from direct to indirect in going from the ML to the BL, the resonant Raman conditions also change. WS₂ shows a strong spin—orbit interaction with a value of 0.39 eV that allows exciton—phonon resonance features to appear spectrally.²⁵ Large energetic separation of excitons allows observation of the redshifts of the A exciton and the blue shift of the B exciton in the absorption spectra for BLs. These exciton shifts are not significantly large but still result in a change in the electronic band structure (Figure 3a). Excitons are confined in the plane of the monolayer, but in bilayers, the excitonic wave functions near high-energy C excitons overlap in momentum space. This can lead to the appearance of an increased number of phonon modes (Figure 3b). Hence, Raman spectra as a function of laser energy excitation allow us to understand the spectral features

corresponding to phonon interactions in layered TMDs and the strength of coupling of excitons and phonons.

2.3. Raman Spectroscopy. Raman spectroscopy measures inelastic scatterings of phonons, which provides a quick, nondestructive, and noninvasive method for characterizing thickness, crystallinity, and interlayer interactions in 2D materials. Raman scattering experiments can also measure the energy of a specific phonon mode of a crystal that is Raman-active by vibrational symmetry. Polarized Raman spectra of TMDs as a function of laser excitation energy allow us to understand the dependence of the scattering intensity on the crystal symmetry and polarization-dependent Raman tensor of phonon modes in TMDs. In the case of polarized Raman spectroscopy, the polarization of the incident photons and the scattered photons is controlled such that the selection rules for Raman scattering from phonon modes allow accurate

mode assignments, which is not always possible in unpolarized Raman measurements. The intensity of the Raman mode can be described as $I \propto |\mathbf{e_s} \cdot \mathcal{R} \cdot \mathbf{e_i}|$, where \mathcal{R} is the Raman tensor of the vibration mode, and e_i and e_s are the polarization vectors of the incident and scattered photons, respectively. If the polarization of the incident and scattered photons has an angle between them (e.g., $e_i = (\sin \beta, \cos \beta, 0)$, $e_s = (0,1,0)$), then the intensity of the Raman tensor for shear modes will have β -dependence, while the breathing modes will be independent of β where $\beta = 0^\circ$ for parallel and $\beta = 90^\circ$ for cross-polarization.

Ultralow-frequency (ULF) Raman modes can reveal interlayer interactions as they correspond to the vibrations of constituent layers. The individual layer is a large ensemble of atoms that experiences intralayer restoring forces within its layer. In contrast, weak vdWs forces between two layers result in low-frequency (LF) Raman peaks, depending on the stacking angle. The LF and ULF modes lie below 100 and 50 cm⁻¹, respectively. The interlayer ULF modes can be divided into in-plane shear (S) and out-of-plane breathing (B) vibration modes with dependencies on excitation polarization. Because these modes are susceptible to interlayer coupling, they can be used not only for measuring layer thickness but also for probing the effects of the twist angle on the vibrational modes. Twist angle-dependent ULF remains largely unexplored in TMD homostructures because ULF modes are hardly observed because they are in close vicinity of the Rayleigh background.²⁹ By using resonant laser excitation, we can probe these ULF modes. Figure 4 shows the laser excitation-dependent low-frequency Raman spectra (LFRS) of monolayer and bilayer WS2 with no twist angle. In the case of the WS₂ ML at a laser excitation energy of 2.34 eV, the peak at 28 cm⁻¹ (Figure 4a) is the second-order longitudinal acoustic (LA) mode due to the interaction with the substrate.³⁰ These polarized Raman spectra were obtained with the linear polarization direction of scattered light parallel (XX configuration) or perpendicular (XY cross-configuration) to that of the incident excitation beam, as shown in the Supporting Information (Figure S4). For the BL, the narrow peak at \sim 28.0 cm⁻¹ can be detected only in the cross-polarization, thus identified as a B mode (Figure 4a). A much weaker peak at ~46 cm⁻¹ corresponds to the interlayer S mode since it is observed in both XX and XY polarizations. Figure 4b shows that when the laser excitation energy (2.54 eV) is close to the B exciton resonance, the intensities of peaks get enhanced near resonances because of the interactions of phonons with the B exciton states. The 2L shows more spectral features, with a peak at 17.6 cm⁻¹ corresponding to the S mode, another peak at 21.6 cm⁻¹ corresponding to the B mode, and a final peak at 31 cm⁻¹ corresponding to the transverse acoustic TA phonon

Figure 5 shows the LFRS for the WS_2 BL with different twist angles. The mode at 28 cm^{-1} is present in all of the cases of twisted bilayers and monolayers, while the mode at 46 cm^{-1} is absent in monolayers (Figure 5a). The improved interlayer coupling due to the annealing of artificially stacked samples is confirmed by the presence of a mode at 46 cm^{-1} . The mode at 46 cm^{-1} could be attributed to the weak scattering cross-section and low-intensity second-order LA modes in the BL.³¹

Our results confirm that the intensity of interlayer S modes in bilayers is more sensitive to the interlayer separation distance compared to the interlayer B modes. The force constants for B modes are less sensitive to the lattice mismatch present in the homobilayers. Therefore, we mainly observe the interlayer B modes for homobilayers. Both S and B modes in the ULF range are sensitive to the twist angle in bilayers. The LA and B modes shift by 1 cm⁻¹ wavenumber in bilayers compared with monolayers, indicating that the layers in the twisted structures are not electronically decoupled in the out-of-plane direction. The prominent peak corresponding to the B mode is clearly visible in Figure 5a, while the S mode is hardly observable due to the weak intensity.

Figure 5b shows the two prominent peaks at around 356 and 419 cm⁻¹. The typical phonon modes of E_{2g}^1 and A_{1g} at the Γ -point with frequency separations of 61 cm⁻¹ are observed in the pristine \overline{WS}_2 monolayer. The position of E^1_{2g} peaks is not sensitive to twist angles, while the A_{1g} peaks shift with the twist angles, being consistent with the previous results.³³ The softening of A_{1g} phonons with increasing twist angle indicates that the interlayer coupling is strongest for small twist angles. Twisted bilayers of TMDs can introduce periodic potential that can modify the dynamics of interacting layers to generate moiré phonons within the superlattice. Moiré phonons are inactive in natural bilayers but become active in artificially stacked twisted bilayers due to the folding of the phonon bands by the moiré superlattice.³⁴ Figure 5c shows folded acoustic and optical moiré phonons reflected in the Raman spectra of twisted bilayers. The appearance of moiré phonons for a range of twist angles gives rise to the localization of electronic states and the enhancement of electron-electron interactions, signifying the strong interlayer coupling.

The splitting of the A_{1g} Raman mode, denoted as FA_{1g} , stems from the off-center phonons of the monolayer coupled with the lattice vectors of the moiré reciprocal space (Figure 5c). The moiré phonons FA1g at different twist angles are derived from distinct different wave vectors of the phonon dispersion. The frequency and intensity of FA1g modes also depend on the twist angles. The trend in Raman spectra shows that FA₁₀ modes red-shift until the twist angle of 3° and then remain nearly constant until the twist angle of 30°. Figure 5d,e shows the peak position of E^1_{2g} , A_{1g} phonon modes and frequency separation between the E^1_{2g} (Γ) and A_{1g} (Γ) phonon modes $(\omega_A - \omega_E)$ as a function of the twist angle. The peak positions are determined by Lorentz fitting in Raman spectra [Figure S2]. E_{2g}^1 mode red-shifts going from the monolayer to the bilayer. The variation of the E_{2g}^1 mode with the twist angle is not significant; it slightly changes for different twist angles, while A_{lg} shows better dependence. The frequency separation and position of the A_{1g} mode can be used to characterize the effective interlayer coupling strength. The strength of interlayer coupling can be used in determining the interlayer distance, which is defined as the distance between the planes of W atoms in separate layers. In bilayers, the two energetically stable, high-symmetry stackings are AA (twist angle of 0) and AB (twist angle of 60). The DFT calculations show that the value of interlayer distance for AA and AB stackings is 6.21 and 6.42 nm, respectively.³⁵ For twisted bilayers, interlayer distances are between the maximum and minimum values of high-symmetry stacking, suggesting strong interlayer coupling. The interlayer distance in twisted systems varies with the twist angle because of symmetry reduction and steric repulsion effects.^{35–37} If interfacial coupling weakens with the twist angle, this leads to larger interlayer distances, softened in-plane modes, and stiffened out-of-plane modes.³⁸ A large twist angle implies an increased interlayer distance and weak coupling. We summarized the peak position of the $E_{2g}^1(\Gamma)$ and $A_{1g}(\Gamma)$ in

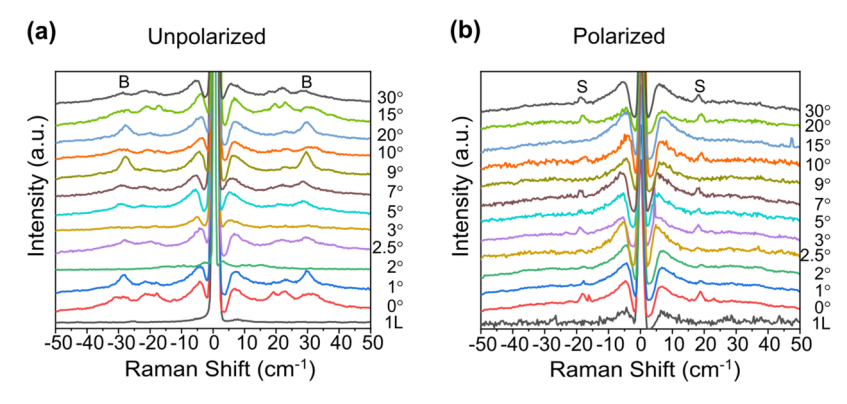


Figure 6. (a) Unpolarized low-frequency Raman spectra of the monolayer compared to bilayers having a range of twist angles with a laser excitation of 488 nm (2.54 eV) and (b) cross-polarized configuration of polarization Raman spectra as a function of the twist angle. In the cross-polarization configuration, the interlayer B mode is suppressed, and the S mode is more prominent.

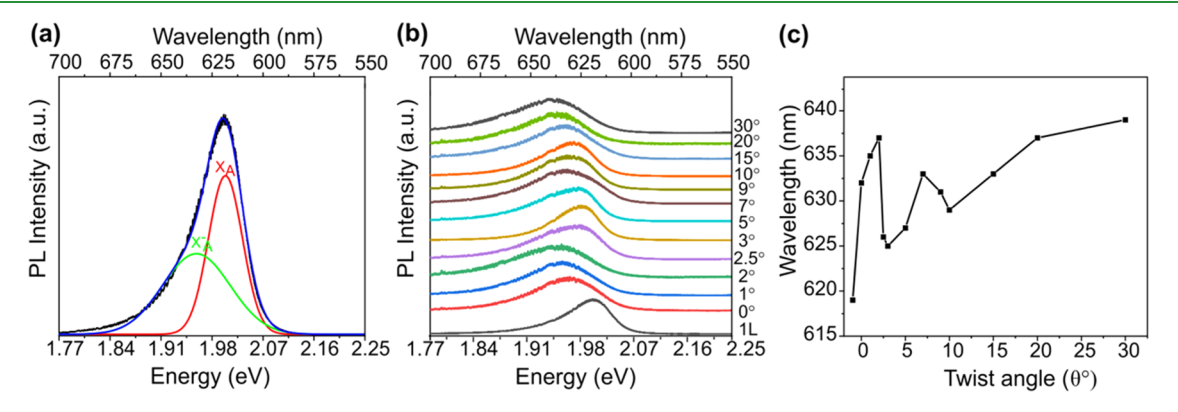


Figure 7. (a) PL spectra of pristine monolayer WS₂. The red and green curves show the results of multiple peaks fit with the Lorentzian function. For pristine WS₂, trions (X_A^{-1}) and neutral excitons (X_A) are located at 1.98 and 2.02 eV, respectively. (b) PL of differently twisted bilayers in comparison to the monolayer. The intensity of photoluminescence decreases going from the monolayer to the bilayer. (c) Shift of the direct band gap.

Figures 5d and the corresponding frequency separation as a function of twist angles in Figure 5d,e, respectively. We observe that the E^1_{2g} and A_{1g} modes are sensitive to the twist angle, and their fluctuation is dependent on interlayer coupling. Previous work has shown that the moiré lattice can be divided into three different regimes of relaxed, rigid, and transition (twist angle < 6°) lattice.³⁹ In the transition regime, the fluctuation of high-frequency Raman modes in terms of line width and position is more visible. The largest separation of 63.23 cm⁻¹ is achieved at a twist angle of 2°, which indicates strong interlayer coupling in the transition regime (Figure 5e).

To confirm the strength of the interfacial coupling of our samples, we performed polarized Raman spectroscopy in the ULF region (Figure 6). In our results, under the unpolarized Raman configuration, the S mode disappears above 2° and reappears again at 20 and 30°. When the two layers of a TMD are rotated 180° with respect to each other, the most stable stacking 2H (or AB stacking) is obtained.⁴⁰ In natural homobilayers, commensurate 2H stacking is mostly present. Meanwhile, in twisted bilayers, a lattice mismatch appears due to the twist angle, creating an incommensurate lattice structure. As the two adjacent layers are bound together by the weak vdWs interaction, the interlayer coupling in ±K valleys can be largely suppressed by the giant spin-orbit splitting.⁴¹ The reappearance of the S modes at large angles can be understood in terms of the lack of commensurate lattice and weak interlayer coupling. 32,42 The observation of the same interlayer (B) and (S) mode frequencies for the twisted bilayer

WS₂ with twist angles smaller than 3° provides evidence of atomic reconstruction (i.e., rearrangement of atoms within the individual layers). The formation of a moiré pattern is expected to cause atomic reconstruction and is largely influenced by the competition between strain and interlayer coupling at different twist angles.³⁴ For small twist angles (<3°), bilayers will try to achieve stable stacking (2H), and hence, the atomic reconstruction causes softening of modes, demonstrating strong interlayer coupling. When the twist angle rises above the threshold angle (>2°), the reconstruction no longer occurs, and the moiré superlattice becomes stable.³⁴ This stability leads to a significant softening of the interlayer B mode because the moiré superlattice creates periodic modulations in the lattice and results in the mixing of the in-plane and out-ofplane modes. This mode then stiffens again with a decreasing moiré period or increasing twist angle because of strain in the lattice. In our results, the interlayer B mode shows the change in terms of varied intensity, line width, and shift in the mode position depending on the twist angles.

The Raman measurements reveal that the interlayer (B) and (S) modes shift significantly with small twist angles, demonstrating their sensitivity to the interlayer stacking and coupling strength. In contrast, for twist angles between 9 and 15° where the stacking is found to yield mismatched lattices without any moiré superlattices, the S mode is not observed because its effects are expected to occur at very low frequency (<10 cm⁻¹). The appearance of the very LF spectral features (in terms of intensity) is because of the in-plane layer—layer

shear vibrations that lead to virtually no restoring forces associated with the mismatched stacking (i.e., very weak interlayer shear coupling).

2.4. Photoluminescence Measurements. We used photoluminescence (PL) characterizations to further probe the optical properties of the twisted bilayer WS2 as a function of twist angles. Figure 7a shows a much higher PL intensity for monolayer WS₂ compared to the bilayer WS₂ because of the direct-to-indirect band gap transition. A single peak corresponding to the A exciton resonance at \sim 619 nm (2 eV) is observed for the monolayer (Figure 7a). The PL in the monolayer originates from the direct exciton transition between the conduction band minimum and the valence band maximum (VBM). The PL intensity is slightly asymmetric, indicating the presence of trions in addition to neutral excitons.43 The high-energy component of PL corresponds to excitons, whereas the tail of the PL at slightly lower energy corresponds to negatively charged trions whose binding energies are tens of meV (Figure 7a). In contrast, the PL spectra of the bilayer show a decrease in intensity and a much broader peak. Energy and charge transfers are the main reasons for reducing the PL intensity in bilayer WS₂.³⁸ The exciton dynamics in TMDs can also be influenced by ambiance factors, such as temperature. At low temperatures, dark exciton states are present in TMDs, which cannot recombine directly and thus quench PL intensity. 44 In addition, with an increase in temperature, the PL intensity of the moiré exciton rapidly decreases and disappears at temperatures higher than ~30 K. In twisted bilayers, the TMD moiré potential also influences exciton dynamics and exciton radiative lifetimes. This is mainly because the thermal energy is greater than the trapping potential energy, and the exciton-bound state undergoes thermal dissociation assisted by thermal excitation. 45,46 Interestingly, recent ultrafast pump-probe experiments suggest that their lifetime is mostly temperature-independent, although the lifetime of charge carriers increases from a few tens of picoseconds to more than a nanosecond going from the monolayer to a few layers.47

In homobilayers, electron transfer occurs between states with the same energy. In the case of heterobilayers, charge transfer is more prominent as electrons and holes are spatially separated in each layer. However, in homobilayers, the energy transfer is significant. In the band structure, the conduction band is dominated by the d-orbitals of W atoms and the valence band by the p-orbitals of S atoms. The changing interlayer interaction with changing twist angles causes variations for both orbitals and thus leads to band shifting in bilayers. Depending on the twist angle, the continuous shift in PL indicates a change in the indirect band gap energy (Figure 7b). More excitons are relaxed through the indirect pathways rather than direct K-K transition, hence lowering the total PL intensity. For the small range of twist angles, the PL peak shows a large redshift, and the maximum redshift is at 2°. In the case of small twist angle bilayers, the separation between top and bottom monolayers is a minimum compared to the large twist angles of bilayers. The minimum separation at small twist angles strengthens the interlayer coupling. The constant position of B and S modes in the phonon spectra up to 2° also supports the interpretation of the lattice reconstruction. This reconstruction is also seen in the stable stacking. After 2°, the moiré period is stable, and the modulations in the electronic structure induced by the periodic potential are reflected by the blue shifts in PL peak positions with small variation. The

trends in PL spectra are consistent with the phonon dispersion, suggesting that the strongest interlayer coupling occurs at a small but nonzero twist angle (Figure 7c). However, for twist angles greater than 10°, PL red-shifts significantly because of the weakened interlayer coupling. We observed higher PL intensity peaks at twist angles of 30° and 10° and much weaker and broader peaks at 2° and 20°. This variation in intensity with the twist angle can be attributed to the strength of interlayer coupling and interlayer distance. For example, the low PL intensity is because of the strong interlayer interaction from the minimized steric effect.³⁷ The value of the direct band gap is known to remain constant when the twist angle of bilayer TMDs changes. 40 However, in our PL measurement, shifts in the peak position as much as 15 nm were observed with changing twist angles (Figure 7b). This peak shift in PL is also reported in similar studies. 36,37,46 One possible explanation is that the variation of the PL line depends on the contribution of trions and excitons excited in the monolayer.⁴³ The PL peaks of the direct band gap are the convolution of excitons (X_A) and trions (X_A^{-1}) (Figure 7a). In this explanation, the strength of the interlayer interaction changing with the twist angles is supposed to cause changes in relative intensities of trions and excitons. Ji et al. reported the PL spectra of homobilayers dominated by dynamics of excitons and trions. In this work, the binding energy of trions is dependent on the twist angle, which influences the shape of the convoluted PL peak.^{37,48} Furthermore, the absorption spectra (Figure S3) show the position shift of the A exciton depending on the twist angle and thus support the peak shift seen in our PL results. Another possible reason for the shift in the PL peak is that mechanical strain is an expected factor in twisted bilayers of WS₂, which can affect its band gap, high-frequency phonons, and excitonic states, resulting in a shift in the photoluminescence (PL) peak. The twist angle changes the crystallographic directions between the bilayers, also causing strain. Although strain lowers the band gap in twisted TMDs, the weaker interactions between twisted bilayers at large twist angles can also contribute to lowering the band gap. 35 Thus, it is difficult to estimate the origin and the relative magnitude of the strain and quantitatively attribute it to the observed variations in the PL shift. Importantly, we do not observe the splitting of E_{2g}^1 phonons in Raman spectra, indicating that the effect of mechanical strain is minimal.³⁹ Also, the annealing method used in our bilayer fabrication supports minimizing strain effects observed in the PL shift.⁴⁹ Additional experiments and theoretical calculations may be needed to gain a deeper understanding of the results pertaining to the trends in the PL spectra.

3. CONCLUSIONS

In this work, we have demonstrated that Raman phonon modes are efficient probes in understanding the strength of moiré phonons arising in twisted bilayer TMDs. Resonant Raman scattering reveals distinct spectral features of the LF phonons. Scanning from a small twist angle to a large angle, there is a consistent shift in the characteristic modes, implying softening and stiffening of the modes. In contrast to the ULF interlayer Raman modes, the high-frequency modes are much less sensitive to interlayer stacking and coupling; the maximum variation in frequency is about 1 cm⁻¹ in bilayers, depending on the twist angle. The interlayer B modes show small variations with different twist angles, as the mismatched stacking leads to almost constant interlayer B mode coupling.

In cases where the number of multiple B modes increases, their origin indicates nonuniform coupling across the interface because of transfer-induced localized strains. Specifically, polarized Raman spectroscopy can identify the S modes observed in the cases of twisted bilayers, implying a strong interaction in bilayers. Because of the clean and large interfaces of stacking monolayers, the LF modes are clearly visible in most twisted bilayer samples. The PL results shed light on the trend of trions and neutral excitons in bilayers, depending on the twist angle. The etchant-free transfer of TMD monolayers may provide high-quality van der Waals interfaces and well-controlled twist angles for the fabrication of advanced optoelectronic devices using twisted bilayer TMDs.

4. METHODS

4.1. Metal-Organic Chemical Vapor Deposition (MOCVD) Growth. The WS₂ monolayers used in preparing van der Waals structures are coalesced unidirectional films grown on a 2 in.-diameter c-plane sapphire substrate. The WS₂ samples were grown using a multistep metal-organic chemical vapor deposition (MOCVD) technique involving the nucleation, ripening, and lateral growth of domains. A cold-wall, horizontal, low-pressure MOCVD reactor was used for the growth. The multistep growth started with the first step of heating the sapphire substrate to the nucleation temperature between 850 and 1000 °C under an H2 carrier gas flow. In the second step, the gaseous precursors W(CO)₆ and H₂S were introduced at 1000 °C, with the ripening of triangular domains of WS₂. 19 Ripening refers to the surface diffusion of W-rich adatoms or the migration of W-rich WS_x clusters. The nucleation and ripening steps provide a means to control the density, size, and orientation of WS2 islands, which are essential for achieving coalesced monolayer films. After the growth, as the third step, the sample was annealed in H2S for a few more minutes to compensate for desulfurization. This step is followed by cooling the sample to 300 °C to avoid WS₂ decomposition. Finally, a high-quality, high-grain, boundary-free epitaxial film of WS₂ is ready to use for the characterization and transfer process.

4.2. Absorption, Raman, and PL Measurements. The optical absorption measurements were performed using an Agilent UV—vis-NIR spectrophotometer. Raman measurements were performed by using a HORIBA LabRAM HR Evolution Raman microscope with laser wavelengths of 532 and 488 nm (ULF). For Raman and PL measurements, a grating with 1800 grooves per mm and 300 grooves per mm was employed. Before the measurements, the system was aligned well and calibrated with the Raman peak of Si at 520 cm⁻¹. Raman WS₂ signature positions, as well as the position and intensity of the near band gap emission in PL from WS₂ were mainly used to confirm the formation of monolayer films.

4.3. AFM Measurements. A Bruker Icon atomic force microscope (AFM) was used to study the surface morphology, domain size, coverage, and thickness of the deposited layers. Scanasyst air probe AFM tips with a nominal tip radius of \sim 2 nm and spring constant of 0.4 N/m were employed for the measurements, and images were collected using peak-force tapping mode.

ASSOCIATED CONTENT

Supporting Information

The Supporting Information is available free of charge at https://pubs.acs.org/doi/10.1021/acsami.3c14708.

Etchant-free method of controlling the twist angle, peak fit Raman spectra for the WS₂ bilayer at 30° twist angle, and absorption spectra and polarized Raman spectra of monolayer and bilayer WS₂ at varying twist angles (PDF)

AUTHOR INFORMATION

Corresponding Author

Jae Yong Suh — Department of Physics, Michigan Technological University, Houghton, Michigan 49931, United States; ⊚ orcid.org/0000-0001-9357-5935; Email: jsuh@mtu.edu

Authors

Manpreet Boora – Department of Physics, Michigan Technological University, Houghton, Michigan 49931, United States

Yu-Chuan Lin — Department of Materials Science and Engineering, The Pennsylvania State University, University Park, Pennsylvania 16802, United States; Department of Materials Science and Engineering, National Yang Ming Chiao Tung University, Hsinchu City 300093, Taiwan; orcid.org/0000-0003-4958-5073

Chen Chen – Department of Materials Science and Engineering, The Pennsylvania State University, University Park, Pennsylvania 16802, United States

Nicholas Trainor – Department of Materials Science and Engineering, The Pennsylvania State University, University Park, Pennsylvania 16802, United States

Joshua A. Robinson — Department of Materials Science and Engineering, The Pennsylvania State University, University Park, Pennsylvania 16802, United States; 2D Crystal Consortium Materials Innovation Platform, The Pennsylvania State University, University Park, Pennsylvania 16802, United States; Department of Chemistry and Department of Physics, The Pennsylvania State University, University Park, Pennsylvania 16802, United States;

orcid.org/0000-0002-1513-7187

Joan M. Redwing — Department of Materials Science and Engineering, The Pennsylvania State University, University Park, Pennsylvania 16802, United States; 2D Crystal Consortium Materials Innovation Platform, The Pennsylvania State University, University Park, Pennsylvania 16802, United States; orcid.org/0000-0002-7906-452X

Complete contact information is available at: https://pubs.acs.org/10.1021/acsami.3c14708

Notes

The authors declare no competing financial interest.

ACKNOWLEDGMENTS

The authors thank Prof. J.A.R. for giving valuable feedback during meetings and providing his lab space for working on transfers. The authors thank Prof. J.M.R. for overseeing the progress of the project. The authors also thank Maxwell T. Wetherington for training and assisting with a set of Raman measurements. The authors also thank Kyle Thomas Munson and Shreya Mathela for their time and insightful discussions on exciton dynamics and for conducting the transient absorption measurements. The WS₂ monolayers and transfer stage for stacking bilayers for this publication were provided by the Pennsylvania State University Two-Dimensional Crystal Consortium – Materials Innovation Platform (2DCC-MIP) under the Resident Scholar Visitor Program (RSVP), which is supported by NSF grants DMR-1539916 and DMR-2039351. Y.-C.L. thanks the Yushan Fellow Program by the Ministry of Education (MOE), Taiwan, for the financial support.

REFERENCES

- (1) Lisi, S.; Lu, X.; Benschop, T.; de Jong, T. A.; Stepanov, P.; Duran, J. R.; Margot, F.; Cucchi, I.; Cappelli, E.; Hunter, A.; Tamai, A.; Kandyba, V.; Giampietri, A.; Barinov, A.; Jobst, J.; Stalman, V.; Leeuwenhoek, M.; Watanabe, K.; Taniguchi, T.; Rademaker, L.; van der Molen, J.; Allan, M. P.; Efetof, D. K.; Baumberger, F. Observation of Flat Bands in Twisted Bilayer Graphene. *Nat. Phys.* **2021**, *17* (2), 189–193.
- (2) Zeng, H.; Cui, X. An Optical Spectroscopic Study on Two-dimensional Group-VI Transition Metal Dichalcogenides. *Chem. Soc. Rev.* **2015**, *44* (9), 2629–2642.
- (3) Huang, X.; Zeng, Z.; Zhang, H. Metal Dichalcogenide Nanosheets: Preparation, Properties and Applications. *Chem. Soc. Rev.* 2013, 42 (5), 1934–1946.
- (4) Malard, L. M.; Alencar, T. V.; Barboza, A. P. M.; Mak, K. F.; De Paula, A. M. Observation of Intense Second Harmonic Generation from MoS₂ Atomic Crystals. *Phys. Rev. B* **2013**, 87 (20), No. 201401.
- (5) Zhang, X.; Qiao, X. F.; Shi, W.; Wu, J. B.; Jiang, D. S.; Tan, P. H. Phonon and Raman Scattering of Two-Dimensional Transition Metal Dichalcogenides from Monolayer, Multilayer to Bulk Material. *Chem. Soc. Rev.* **2015**, *44* (9), 2757–2785.
- (6) Li, H.; Shi, Y.; Chiu, M. H.; Li, L. J. Emerging Energy Applications of Two-Dimensional Layered Transition Metal Dichalcogenides. *Nano Energy* **2015**, *18*, 293–305.
- (7) Zhang, X.; Zhang, R.; Zheng, X.; Zhang, Y.; Zhang, X.; Deng, C.; Qin, S.; Yang, H. Interlayer Difference of Bilayer-Stacked MoS₂ Structure: Probing by Photoluminescence and Raman Spectroscopy. *Nanomaterials* **2019**, *9* (5), No. 796.
- (8) Cong, C.; Shang, J.; Wang, Y.; Yu, T. Optical Properties of 2D Semiconductor WS₂. Adv. Opt. Mater. **2018**, 6 (1), No. 1700767.
- (9) Ovchinnikov, D.; Allain, A.; Huang, Y. S.; Dumcenco, D.; Kis, A. Electrical Transport Properties of Single-Layer WS₂. ACS Nano **2014**, 8 (8), 8174–8181.
- (10) Falin, A.; Holwill, M.; Lv, H.; Gan, W.; Cheng, J.; Zhang, R.; Qian, D.; Barnett, M. R.; Santos, E. J. G.; Novoselov, K. S.; Tao, T.; Wu, X. W.; Li, L. H. Mechanical properties of atomically thin tungsten dichalcogenides: WS₂, WSe₂, and WTe₂. ACS Nano **2021**, 15 (2), 2600–2610.
- (11) Zeng, H.; Liu, G. B.; Dai, J.; Yan, Y.; Zhu, B.; He, R.; Xie, L.; Xu, S.; Chen, X.; Yao, W.; Cui, X. Optical Signature of Symmetry Variations and Spin-valley Coupling in Atomically Thin Tungsten Dichalcogenides. *Sci. Rep.* **2013**, *3* (1), No. 1608.
- (12) Choi, J.; Florian, M.; Steinhoff, A.; Erben, D.; Tran, K.; Kim, D. S.; Sun, L.; Quan, J.; Claassen, R.; Majumder, S.; Hollingsworth, J. A.; Taniguchi, T.; Watanabe, K.; Ueno, K.; Singh, A.; Moody, G.; Jahnke, F.; Li, X. Twist Angle-Dependent Interlayer Exciton Lifetimes in van der Waals Heterostructures. *Phys. Rev. Lett.* **2021**, *126* (4), No. 047401.
- (13) Bistritzer, R.; MacDonald, A. H. Moiré Bands in Twisted Double-Layer Graphene. *Proc. Natl. Acad. Sci. U.S.A.* **2011**, *108* (30), 12233–12237.
- (14) Tran, K.; Moody, G.; Wu, F.; Lu, X.; Choi, J.; Kim, K.; Rai, A.; Sanchez, D. A.; Quan, J.; Singh, A.; Embley, J.; Zepeda, A.; Campbell, M.; Autry, T.; Taniguchi, T.; Watanabe, K.; Lu, N.; Banerjee, S. K.; Silverman, K. L.; Kim, S.; Tutuc, E.; Yang, L.; MacDonald, A. H.; Li, X. Evidence for Moiré Excitons in van der Waals Heterostructures. *Nature* 2019, 567 (7746), 71–75.
- (15) Koshino, M.; Yuan, N. F.; Koretsune, T.; Ochi, M.; Kuroki, K.; Fu, L. Maximally Localized Wannier Orbitals and the Extended Hubbard Model for Twisted Bilayer Graphene. *Phys. Rev. X* **2018**, 8 (3), No. 031087.
- (16) Hamer, M. J.; Giampietri, A.; Kandyba, V.; Genuzio, F.; Menteş, T. O.; Locatelli, A.; Gorbachev, R. V.; Barinov, A.; Mucha-Kruczyński, M. Moiré Superlattice Effects and Band Structure Evolution in Near-30-Degree Twisted Bilayer Graphene. ACS Nano 2022, 16 (2), 1954–1962.
- (17) Liao, M.; Wei, Z.; Du, L.; Wang, Q.; Tang, J.; Yu, H.; Wu, F.; Zhao, J.; Xu, X.; Han, B.; Liu, K.; Gao, P.; Polcar, T.; Sun, Z.; Shi, D.; Yang, R.; Zhang, G. Precise Control of the Interlayer Twist Angle in

- Large Scale MoS₂ Homostructures. Nat. Commun. 2020, 11 (1), No. 2153.
- (18) Li, M.; Yang, Y.; Yu, D.; Li, W.; Ning, X.; Wan, R.; Zhu, H.; Mao, J. Recent Advances on the Construction of Encapsulated Catalyst for Catalytic Applications. *Nano Res.* **2023**, *16* (2), 3451–3474.
- (19) Chubarov, M.; Choudhury, T. H.; Hickey, D. R.; Bachu, S.; Zhang, T.; Sebastian, A.; Bandsal, A.; Zhu, H.; Trainor, N.; Das, S.; Terroncio, M.; Alem, N.; Redwing, J. M. Wafer-scale Epitaxial Growth of Unidirectional WS₂ Monolayers on Sapphire. *ACS Nano* **2021**, *15* (2), 2532–2541.
- (20) Amani, M.; Chin, M. L.; Mazzoni, A. L.; Burke, R. A.; Najmaei, S.; Ajayan, P. M.; Lou, J.; Dubey, M. Growth-substrate Induced Performance Degradation in Chemically Synthesized Monolayer MoS₂ Field Effect Transistors. *Appl. Phys. Lett.* **2014**, *104* (20), No. 203506.
- (21) Lin, Z.; Zhao, Y.; Zhou, C.; Zhong, R.; Wang, X.; Tsang, Y. H.; Chai, Y. Controllable Growth of Large—size Crystalline MoS₂ and Resist-free Transfer Assisted with a Cu Thin Film. Sci. Rep. 2015, 5 (1), No. 18596.
- (22) Zhu, B.; Chen, X.; Cui, X. Exciton Binding Energy of Monolayer WS₂. Sci. Rep. **2015**, 5 (1), No. 9218.
- (23) Mennel, L.; Smejkal, V.; Linhart, L.; Burgdörfer, J.; Libisch, F.; Mueller, T. Band Nesting in Two-dimensional Crystals: An Exceptionally Sensitive Probe of Strain. *Nano Lett.* **2020**, *20* (6), 4242–4248.
- (24) Yuan, N. F.; Isobe, H.; Fu, L. Magic of High-order van Hove Singularity. *Nat. Commun.* **2019**, *10* (1), No. 5769.
- (25) Chernikov, A.; Berkelbach, T. C.; Hill, H. M.; Rigosi, A.; Li, Y.; Aslan, B.; Reichman, D. R.; Hybertsen, M. S.; Heinz, T. F. Exciton Binding Energy and Nonhydrogenic Rydberg Series in Monolayer WS₂. *Phys. Rev. Lett.* **2014**, *113* (7), No. 076802.
- (26) Berkdemir, A.; Gutiérrez, H. R.; Botello-Méndez, A. R.; Perea-López, N.; Elías, A. L.; Chia, C. I.; Wang, B.; Crespi, V. H.; Lopez-Urias, F.; Charlier, J. C.; Terrones, H.; Terrones, M. Identification of Individual and Few Layers of using WS₂ Raman Spectroscopy. *Sci. Rep.* **2013**, 3 (1), No. 1755.
- (27) Lee, J. U.; Cheong, H. Resonance Raman Effects in Transition Metal Dichalcogenides. *J. Raman Spectrosc.* **2018**, 49 (1), 66–75.
- (28) Tan, Q. H.; Sun, Y. J.; Liu, X. L.; Xu, K. X.; Gao, Y. F.; Ren, S. L.; Tan, P. H.; Zhang, J. Breakdown of Raman Selection Rules by Fröhlich Interaction in Few-layer WS₂. *Nano Res.* **2021**, *14*, 239–244.
- (29) Yang, J.; Lee, J. U.; Cheong, H. Excitation Energy Dependence of Raman Spectra of Few-layer WS₂. FlatChem **2017**, *3*, 64–70.
- (30) Xiang, Q.; Yue, X.; Wang, Y.; Du, B.; Chen, J.; Zhang, S.; Li, G.; Cong, C.; Yu, T.; Li, Q.; Jin, Y. Unveiling the Origin of Anomalous Low-frequency Raman Mode in CVD-grown Monolayer WS₂. *Nano Res.* **2021**, *14* (11), 4314–4320.
- (31) Tan, Q. H.; Sun, Y. J.; Liu, X. L.; Zhao, Y.; Xiong, Q.; Tan, P. H.; Zhang, J. Observation of Forbidden Phonons, Fano Resonance and Dark Excitons by Resonance Raman Scattering in Few-layer WS₂. 2D Mater. **2017**, 4 (3), No. 031007.
- (32) Huang, S.; Liang, L.; Ling, X.; Puretzky, A. A.; Geohegan, D. B.; Sumpter, B. G.; Kong, J.; Meunier, V.; Dresselhaus, M. S. Lowfrequency Interlayer Raman Modes to Probe Interface of Twisted Bilayer WS₂. *Nano Lett.* **2016**, *16* (2), 1435–1444.
- (33) O'Brien, M.; McEvoy, N.; Hanlon, D.; Hallam, T.; Coleman, J. N.; Duesberg, G. S. Mapping of Low-Frequency Raman Modes in CVD-Grown Transition Metal Dichalcogenides: Layer Number, Stacking Orientation and Resonant Effects. *Sci. Rep.* **2016**, *6* (1), No. 19476.
- (34) Lin, K. Q.; Holler, J.; Bauer, J. M.; Parzefall, P.; Scheuck, M.; Peng, B.; Korn, T.; Bange, S.; Lupton, J. M.; Schüller, C. Large-Scale Mapping of Moiré Superlattices by Hyperspectral Raman Imaging. *Adv. Mater.* **2021**, 33 (34), No. 2008333.
- (35) Zhu, Y.; Prezhdo, O. V.; Long, R.; Fang, W.-H. Twist Angle-dependent Intervalley Charge Carrier Transfer and Recombination in Bilayer WS₂. *J. Am. Chem. Soc.* **2023**, *145* (41), 22826–22835.

- (36) Zheng, S.; Sun, L.; Zhou, X.; Liu, F.; Liu, Z.; Shen, Z.; Fan, H. J. Coupling and Interlayer Exciton in Twist-stacked WS₂ bilayers. *Adv. Opt. Mater.* **2015**, 3 (1), 1600–1605.
- (37) Ji, H. G.; Solís-Fernández, P. S.; Erkılıç, U.; Ago, H. Stacking Orientation-dependent Photoluminescence Pathways in Artificially Stacked Bilayer WS₂ Nanosheets Grown by Chemical Vapor Deposition: Implications for Spintronics and Valleytronics. ACS Appl. Nano Mater. 2021, 4 (4), 3717–3724.
- (38) Wei, Y.; Meng, L.; Meng, Z.; Weng, Y.; Kang, L.; Li, X. Probing Angle-Dependent Interlayer Coupling in Twisted Bilayer WS₂. *J. Phys. Chem. C* **2019**, *123* (50), 30684–30688.
- (39) Mallik, S. K.; Sahoo, S.; Sahu, M. C.; Jena, A. K.; Pradhan, G. K.; Sahoo, S. Polarized Moiré Phonon and Strain-coupled Phonon Renormalization in Twisted Bilayer MoS2. *J. Phys. Chem. C* **2022**, *126* (37), 15788–15794.
- (40) Lin, M. L.; Tan, Q. H.; Wu, J. B.; Chen, X. S.; Wang, J. H.; Pan, Y. H.; Zhang, X.; Cong, X.; Zhang, J.; Ji, W.; Hu, P. A.; Liu, K. H.; Tan, P. H. Moiré Phonons in Twisted Bilayer MoS₂. ACS Nano **2018**, 12 (8), 8770–8780.
- (41) Zhu, B.; Zeng, H.; Dai, J.; Gong, Z.; Cui, X. Anomalously Robust Valley Polarization and Valley Coherence in Bilayer WS₂. *Proc. Natl. Acad. Sci. U.S.A.* **2014**, *111* (32), 11606–11611.
- (42) Weston, A.; Zou, Y.; Enaldiev, V.; Summerfield, A.; Clark, N.; Zólyomi, V.; Graham, A.; Yelgel, C.; Magrrian, S.; Zhou, M.; Zultak, J.; Hopkinson, D.; Barinov, A.; Bointon, T. H.; Tretinin, A.; Wilson, N. R.; Beton, P. H.; Fal'ko, V. I.; Gorbachev, R. Atomic Reconstruction in Twisted Bilayers of Transition Metal Dichalcogenides. *Nat. Nanotechnol.* **2020**, *15* (7), 592–597.
- (43) Kwon, Y.; Kim, K.; Kim, W.; Ryu, S.; Cheong, H. Variation of Photoluminescence Spectral Line Shape of Monolayer WS₂. *Curr. Appl. Phys.* **2018**, *18* (8), 941–945.
- (44) Bragança, H.; Riche, F.; Qu, F.; Lopez-Richard, V.; Marques, G. E. Dark-Exciton Valley Dynamics in Transition Metal Dichalcogenide Alloy Monolayers. *Sci. Rep.* **2019**, *9* (1), No. 4575.
- (45) Zheng, H.; Wu, B.; Li, S.; Ding, J.; He, J.; Liu, Z.; Wang, C.-T.; Wang, J.-T.; Pan, A.; Liu, Y. Localization-enhanced Moiré Exciton in Twisted Transition Metal Dichalcogenide Heterotrilayer Superlattices. *Light: Sci. Appl.* **2023**, *12* (1), No. 117.
- (46) Barma, P. K.; Upadhyay, P.; Rajarapu, R.; Yadav, S. K.; Latha, K. V. P.; Meenakshisundaram, N.; Nayak, P. K. Twist-dependent Tuning of Excitonic Emissions in Bilayer WSe₂. ACS Omega **2022**, 7 (7), 6412–6418.
- (47) Wang, H.; Zhang, C.; Rana, F. Surface Recombination Limited Lifetimes of Photoexcited Carriers in Few-layer Transition Metal Dichalcogenide MoS₂. Nano Lett. **2015**, 15 (12), 8204–8210.
- (48) Shengxi, H.; Ling, X.; Liang, L.; Kong, J.; Terrones, H.; Meunier, V.; Mildred, S.; Dresselhaus, M. S. Probing the Interlayer Coupling of Twisted Bilayer MoS₂ using Photoluminescence Spectroscopy. *Nano Lett.* **2014**, *14* (10), 5500–5508.
- (49) Zhang, X.; Zhang, R.; Zhang, Y.; Jiang, T.; Deng, C.; Zhang, X.; Qin, S. Tunable Photoluminescence of Bilayer MoS_2 via Interlayer Twist. Opt. Mater. **2019**, 94, 213–216.